Electron-electron interaction in projectile electron loss

H.-P. Hülskötter*
Department of Physics, Stanford University, Stanford, California 94305

B. Feinberg
Accelerator and Fusion Research Division, Lawrence Berkeley Laboratory, One Cyclotron Road, Berkeley, California 94720

W. E. Meyerhof
Department of Physics, Stanford University, Stanford, California 94305

A. Belkacem
Department of Physics, Stanford University, Stanford, California 94305
and Chemical Sciences Division, Building 71-259, Lawrence Berkeley Laboratory, One Cyclotron Road, Berkeley, California 94720

J. R. Alonso
Accelerator and Fusion Research Division, Lawrence Berkeley Laboratory, One Cyclotron Road, Berkeley, California 94720

L. Blumenfeld†
Chemical Sciences Division, Building 71-259, Lawrence Berkeley Laboratory, One Cyclotron Road, Berkeley, California 94720

E. A. Dillard
Department of Physics, Stanford University, Stanford, California 94305

H. Gould
Chemical Sciences Divison, Building 71-259, Lawrence Berkeley Laboratory, One Cyclotron Road, Berkeley, California 94720

N. Guardala‡
Department of Physics, Stanford University, Stanford, California 94305

G. F. Krebs and M. A. McMahan
Accelerator and Fusion Research Division, Lawrence Berkeley Laboratory, One Cyclotron Road, Berkeley, California 94720

M. E. Rhoades-Brown
Accelerator Development Department, Brookhaven National Laboratory, Upton, New York 11973

B. S. Rude
Accelerator and Fusion Research Divison, Lawrence Berkeley Laboratory, One Cyclotron Road, Berkeley, California 94720

J. Schweppe§
Chemical Sciences Division, Building 71-259, Lawrence Berkeley Laboratory, One Cyclotron Road, Berkeley, California 94720

D. W. Spooner
Department of Physics, Stanford University, Stanford, California 94305

K. Street
Berkeley High School, Berkeley, California 94703

P. Thieberger and H. E. Wegner
Department of Physics, Brookhaven National Laboratory, Upton, New York 11973
(Received 17 December 1990)

In ion-atom collisions where the projectile is ionized, target electrons act not only coherently by screening the target nucleus but they may also act incoherently by directly ejecting a projectile electron. This electron-electron interaction should be relatively most important for targets that have a low nuclear charge, since the cross section for a neutral target is roughly proportional to $Z_t^2+Z_t$, where Z_t^2 is the contribution due to the target nucleus and Z_t comes from the target electrons. In order to investigate the electron-electron interaction, we have measured and calculated cross sections for Li^{2+}, C^{5+}, and O^{7+}

on H_2 and He, Au^{52+} on H_2, He, C, and N_2, Au^{75+} on H_2 and N_2, U^{86+} on H_2 and He, and U^{90+} on H_2. The collision energies range from 0.75 to 405 MeV/nucleon. The calculations have been performed in the plane-wave Born approximation. We demonstrate that for energies where the target electrons have sufficient kinetic energy in the projectile frame to ionize the projectile, the electron-electron interaction can lead to a significant increase in the total electron-loss cross section.

I. INTRODUCTION

The subfield of electron-electron interactions within the field of ion-atom collisions has received considerable attention during the last few years. Several different experiments, discussed in the remainder of this section, provide evidence for the existence of electron-electron interactions in ion-atom collisions. This paper concentrates on projectile ionization, here called electron loss to distinguish it from target ionization.

Projectile electron loss is normally attributed to the Coulomb interaction between the target nucleus and a projectile electron. The effect of the target electrons can be accounted for partially by introducing a screened Coulomb interaction between the target and the projectile electron. However, the target electrons can act not only coherently as *screening* agents, but may also act incoherently as ionizing or *antiscreening agents* [1–5]. The antiscreening effect has also been called inelastic electron-electron interaction [6] and two-center electron-electron scattering correlation [7]. This interaction between the target electrons and the projectile electron have a significant effect on the electron-loss cross section, as demonstrated by experiments performed at the Stanford Van de Graaff facility, [8]. Here, cross sections for projectile K-shell electron loss were measured for 0.75–3.5 MeV/nucleon C^{5+} and O^{7+} projectiles in collisions with H_2 and He targets. The experimental results agree with plane-wave Born approximation (PWBA) calculations, but only if the latter take into account the interaction between projectile and target electrons. It has been unambiguously shown that for energies where the target electrons have sufficient kinetic energy in the projectile frame to ionize the projectile, the electron-electron interaction can lead to a significant increase in the total electron-loss cross section. We have now extended these measurements to lithium, gold, and uranium projectiles which together with the previous carbon and oxygen measurements span an energy range from 0.75 to 405 MeV/nucleon and confirm the importance of the electron-electron interaction in ion-atom collisions.

Other experiments that provide evidence for electron-electron interactions involve electron-impact ionization, electron-electron excitation, and electron-electron transfer excitation. Summarizing discussions of all these processes can be found in papers by Stolterfoht [7] and McGuire [9]. Electron-impact ionization experiments [10–12] on ions can be performed by sending a fast-ion beam through a single crystal. Predominantly, silicon crystals have been used for these experiments. The atoms are arranged in a periodic structure with "channels" along which there are no nuclei. With a good alignment of the ion beam, highly charged ions traveling in these channels presumably undergo only large-impact parameter collisions with the distant, screened nuclei and thus should not acquire enough excitation energy to lose their tightly bound electrons. However, the ions will make close collisions with the loosely bound, "quasifree," electrons in the crystal channels. The experimental results clearly show the presence of electron-impact ionization but some of the cross sections cannot be interpreted simply in terms of single-electron impact ionization, as discussed in Ref. [12].

Zouros, Lee, and Richard [13] have been able to provide definite evidence for the Coulomb interaction between target and projectile electrons in projectile inner-shell excitation. In general, it is difficult to distinguish this electron-electron excitation from the electron-nucleus excitation. However, the authors of Ref. [13], using high-resolution, 0° Auger-electron spectroscopy, were able to measure the production cross section for the $(1s2s2p)\,^4P$ state in collisions between O^{5+} and F^{6+} projectiles and a H_2 target. The $(1s2s2p)\,^4P$ state cannot be produced by direct electron-nucleus excitation from the $(1s^22s)\,^2S$ ground state, since this would require a spin-flip transition which is forbidden for these low-Z ions. However, electron-electron excitation can produce the observed state by the exchange of the projectile electron with a target electron. The absolute magnitude of the measured cross sections can be reproduced by an impulse-approximation theory [14].

The transfer-excitation process in ion-atom collisions has been studied intensively in the last several years [15]. Here, a target electron is captured by the projectile and, simultaneously, a projectile electron is excited. In the so-called resonant transfer and excitation process, the projectile electron is excited by the Coulomb interaction with the captured target electron [15]. Schulz *et al.* [16] have found evidence for electron-electron transfer excitation. Here, a collision with a target electron excites the projectile electron and a second, independent, electron is captured by the projectile. The signature for this process is again observed using high-resolution, 0° Auger-electron spectroscopy. The experimental results agree with theoretical estimates within a systematic uncertainty of 50%.

In the following, we begin with a discussion of the electron-loss cross section in the PWBA. The exact calculation of this cross section can be performed only for hydrogenic colliding systems. However, an approximate method allows a calculation for other systems as well. We note that for certain projectile-target combinations it should be possible to demonstrate the screening-antiscreening effect experimentally. Section III contains

the details of the experiments done at Stanford University and the Lawrence Berkeley Laboratory (LBL). Section IV provides some details of the data analysis and Sec. V compares the experimental results with theoretical calculations. This comparison allows us to draw definite conclusions about the significance of the screening-antiscreening effect for projectile electron loss.

II. THEORY

For simplicity, we consider a one-electron projectile p which is ionized by a target t. The extension to many-electron projectiles is straightforward if coherence effects among the projectile electrons are neglected. Using atomic units, the projectile electron-loss cross section in the nonrelativistic PWBA is given by [1–3]

$$\sigma=\frac{8\pi}{v^2}\int_0^\infty d\varepsilon\sum_i\int_{q_{\min}}^{q_{\max}}dq\frac{1}{q^3}|F_p(q)|^2\,|F_t(q,i)|^2\ , \quad (1)$$

where v is the ion velocity, ε the kinetic energy of the ejected projectile electron, and i represents the quantum numbers of the ground and excited (including continuum) states of the target atom. The sum extends over all target states. In the center-of-mass system, the momentum q which is transferred in the collision is defined as the difference between the incoming and outgoing projectile wave vectors, $\mathbf{k}_{\rm in}$ and $\mathbf{k}_{\rm out}$

$$q=|\mathbf{k}_{\rm in}-\mathbf{k}_{\rm out}|\ , \quad (2)$$

where

$$\begin{aligned}k_{\rm in}&=(2MT)^{1/2}\ ,\\ k_{\rm out}&=(2M\{T-[E_g(\text{projectile})+\varepsilon+E_g(\text{target})\\ &\qquad -E_e(\text{target})]\})^{1/2}\ .\end{aligned} \quad (3)$$

The minimum and maximum momentum transfers are given by

$$q_{\min}=k_{\rm in}-k_{\rm out},\quad q_{\max}=k_{\rm in}+k_{\rm out}\ . \quad (4)$$

In Eq. (3), E_g and E_e denote the ground-state and excited-state binding energies, respectively, T is the kinetic energy of the projectile in the center-of-mass system, and M is the reduced mass of projectile and target.

For heavy projectiles, one can make the following approximations for the minimum and maximum momentum transfers [17,18], provided the energy lost in the collision is small compared to the incident kinetic energy T,

$$\begin{aligned}q_{\min}&\simeq[E_g(\text{projectile})+\varepsilon+E_g(\text{target})-E_e(\text{target})]/v\ ,\\ q_{\max}&=\infty\ .\end{aligned} \quad (5)$$

The form factors $F_p(q)$ and $F_t(q,i)$ in Eq. (1) are given by

$$|F_p(q)|^2=|\langle\varepsilon|e^{i\mathbf{q}\cdot\mathbf{r}}|0\rangle_p|^2 \quad (6)$$

and, if the target wave function is written as a product of the individual electron wave functions,

$$|F_t(q,i)|^2=\left|Z_t\delta_{i0}-\sum_j^{N_t}\langle i|e^{i\mathbf{q}\cdot\mathbf{r}_j}|0\rangle_j\right|^2\ . \quad (7)$$

Here Z_t is the target atomic number, δ_{i0} is the Dirac δ function, $|0\rangle_p$ and $|0\rangle_j$ denote the ground-state wave functions of projectile and jth target electron, respectively, $|\varepsilon\rangle$ is the final-state wave function of the ejected projectile electron, $|i\rangle$ is the final-state wave function of the jth target electron, including a possible continuum state, and the sum in Eq. (7) extends over all N_t target electrons. For a neutral target, $N_t=Z_t$.

The projectile form factor $F_p(q)$ involves ground-state and continuum projectile electron wave functions. The continuum-state wave function $|\varepsilon\rangle$ is taken as a projectile-centered Coulomb wave function [1]. For the case of projectile K-shell electron loss, $|F_p(q)|^2$ has been evaluated in closed form by Bethe [19]. If the projectile carries electrons in several shells, the form factor $F_p(q)$ has to be calculated for each individual occupied subshell [20]. The total cross section for electron loss from a many-electron projectile can be obtained by adding the electron-loss cross sections for the individual subshells, weighted by the number of electrons in each subshell. When calculating the individual subshell electron-loss cross sections, one has to take into account the screening of the full projectile nuclear charge by the other inner-shell electrons as well as the screening by the outer, less tightly bound, electrons [17,21].

The target form factor $F_t(q)$ involves target-electron ground-, excited-, and continuum-state wave functions. To evaluate $F_t(q)$ exactly, all these wave functions have to be known. For an atomic hydrogen target, the matrix elements in Eq. (7) have been evaluated exactly by Bates and Griffing [1–3], Bethe, [19], and Chesire and Kyle [22]. Thus for hydrogenic collision systems, the cross section given by Eq. (1) can be calculated exactly within the framework of the PWBA. In general, for hydrogenic as well as nonhydrogenic targets, Eq. (7) can be evaluated in an approximate way, if the target excitation energy $E_g(\text{target})-E_e(\text{target})$ in Eq. (5) is small compared to $E_g(\text{projectile})+\varepsilon$. In the calculations presented in Sec. V, we have replaced the target excitation energy by a mean energy equal to the target ionization energy. Under this condition one can neglect the dependence of the target excitation energy on the final target state i which allows the interchange of the summation over the target ground and excited target states i with the momentum transfer integration in Eq. (1). The resulting cross section can be written as

$$\sigma=\frac{8\pi}{v^2}\int_0^\infty d\varepsilon\int_{q_{\min}}^{q_{\max}}dq\frac{1}{q^3}|F_p(q)|^2S(q,Z_t)\ , \quad (8)$$

where, if closure is used [19], the effective target charge squared $S(q,Z_t)$ is given by

$$\begin{aligned}S(q,Z_t)&=S_s(q,Z_t)+S_a(q,Z_t)\\ &=\left[Z_t-\sum_j^{N_t}F_{jt}(q)\right]^2+\left[N_t-\sum_j^{N_t}|F_{jt}(q)|^2\right]\ .\end{aligned} \quad (9)$$

The two terms in Eq. (9) can be interpreted physically in terms of the ionization by a screened target nucleus (screening) and the ionization by the N_t target electrons (antiscreening). As the momentum transfer q approaches

zero, $F_{jt}(q)\rightarrow 1$, so that for a neutral target where the number of electrons is equal to Z_t the effective perturbing charge vanishes. This situation corresponds to large impact parameters, where the projectile approaches, in effect, a neutral target atom. For high-momentum transfers, or conversely, small-impact parameters, $F_{jt}(q)$ vanishes and $S(q,Z_t)\rightarrow Z_t^2+Z_t$. Therefore, the interaction between target and projectile electrons can result in an increase of the projectile-ionization cross section over the pure nuclear "Born" cross section. The largest relative increase should occur for an atomic hydrogen target where $Z_t=1$. The quantity $\sum_j^{N_t} F_{jt}(q)$ has been tabulated by Hubbell *et al.* [23] for all atoms. For a target with $1s$ electrons, $F_{jt}(q)$ has the analytical form [24]

$$F_{jt}(q)=\frac{1}{[1+(q/2\alpha)^2]^2} , \tag{10}$$

where α is the effective target atomic number. For hydrogen $\alpha=1$ and for helium $\alpha=1.69$, reflecting the screening of the target nucleus by one of the $1s$ electrons.

If one accepts the interpretation that the second term, $S_a(q,Z_t)$ in Eq. (9) represents the ionization by the target electrons, one must take into account the fact that a free electron can eject a projectile electron only if it has sufficient kinetic energy in the projectile's rest frame to do so [18]

$$\tfrac{1}{2}mv^2\geq I , \tag{11}$$

where m is the electron mass, v the relative velocity between the free (target) electron and the projectile, and I the ionization energy of the projectile. This threshold effect is implicit in Eq. (1) through the dependence of $q_{\min}$ on E_e(target), as shown in Eq. (5). This is so because only if a target electron undergoes an inelastic collision, i.e., changes its state, can it transfer momentum to excite or ionize the projectile [2,3]. In the closure approximation, however, the $q_{\min}$ dependence of E_e(target) has been eliminated. To take the threshold effect into account, Anholt proposed the following *ad hoc* correction to $S(q,Z_t)$ [18]

$$S(q,Z_t)=S_s(q,Z_t)+S_a(q,Z_t)[\sigma_e(v)/\sigma_B(v)] , \tag{12}$$

where σ_e is the electron-induced ionization cross section and σ_B is the Born cross section for protons at a velocity equal to the projectile velocity v. The upper limit for the momentum transfer integration in σ_e has to be taken as infinity so that $\sigma_e=\sigma_B$ at high velocities [18].

For Li^{2+}, C^{5+}, and O^{7+} projectiles incident on a helium target we calculated the screening cross sections for the helium nucleus, screened by its two electrons, using $S_s(q,Z_t)$, as well as the sum of the screening and antiscreening cross sections, using $S(q,Z_t)$. Figure 1 shows these cross sections normalized to the "nuclear" PWBA cross section, calculated for a bare helium nucleus. For increasing projectile nuclear charges, the screening cross section approaches the nuclear PWBA cross section. A qualitative explanation for this behavior is that with increasing projectile charge the minimum momentum transfer increases, i.e., the maximum impact parameter decreases. If this maximum impact parameter, above which no projectile ionization can take place, falls significantly below the target K-shell radius, the form factor which characterizes the target electron's screening action approaches zero.

We already mentioned that the largest relative increase in the electron-loss cross section should occur for an atomic hydrogen target. Experimentally, it is difficult to produce a well-understood atomic hydrogen target for collision studies. Therefore, we decided to use a molecular hydrogen target. Although this decision certainly simplifies the experiment, it makes the theoretical calculation more complicated. A quantitative treatment of this problem should include interference terms due to the two scattering centers, the electron correlation within the molecule, and the effect of the spins of the two electrons. The rotational and vibrational degrees of freedom of the molecule can be neglected as long as one considers only molecular ground-state wave functions. A detailed derivation of the PWBA cross section for a H_2 target is given by Meyerhof *et al.* [25] who also discuss several different models for the molecular hydrogen form factor. The main conclusion is that for a projectile of atomic number $Z_p\geq 5$ the molecular-target cross section can be represented by twice the atomic target cross section, but that for $Z_p<5$ molecular effects have to be taken into account. Since the present paper discusses experiments between $Z_p=3$ and 92, we have used for theoretical com-

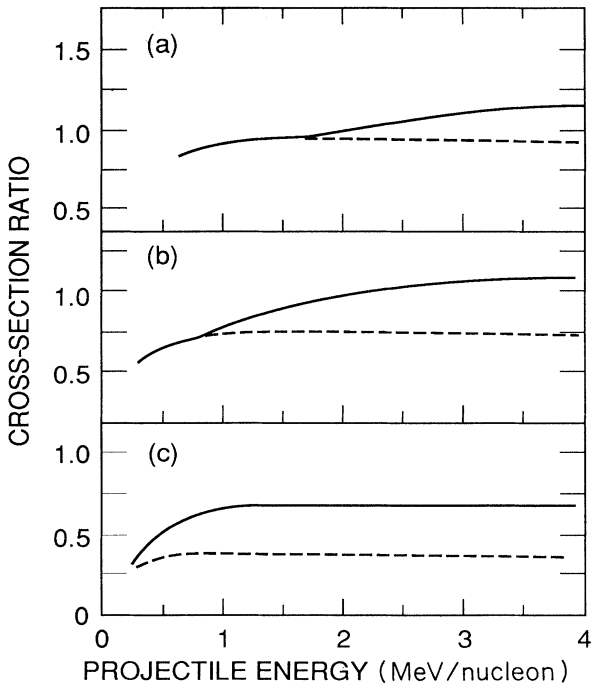

FIG. 1. Calculated K-shell electron-loss cross sections for (a) O^{7+}, (b) C^{5+}, and (c) Li^{2+} projectiles incident on a helium target, normalized to the nuclear PWBA cross section. The dashed line is the scattering cross section, calculated with the first term only in Eq. (12); the solid line is the sum of the screening and antiscreening cross section.

parison one of the molecular H_2 model calculations from Ref. [25]. We decided to use the "Stewart" model which contains a modified form factor $F_{jt}(q)$, Eq. (10), for one electron in the molecule, the interference factor between the two charge centers [26], and the Anholt threshold factor, as in Eq. (12). Use of the latter treats the electron-electron threshold region consistently for H_2 and He targets. We refer to Ref. [25] for details, but note that the Stewart model cross sections differ only little from the Bates-Griffing cross sections for H^0, multiplied by two, except very close to the electron-electron threshold.

III. EXPERIMENTS

This section describes the experimental setups at the Stanford Van de Graaff and the LBL Bevatron accelerators. At the Stanford Van de Graaff accelerator we have measured projectile electron-loss cross sections for Li^{2+}, C^{5+}, and O^{7+} projectiles in collisions with molecular hydrogen and helium targets. The energy ranges from 0.75 to 3.5 MeV/nucleon. Figure 2 shows a schematic of the beam line. Following the charge-state selection by analyzing and switching magnets and, if necessary, post-stripping between the two magnets to obtain the desired charge state, the ion beam is directed into a differentially pumped gas cell after tight collimation and attenuation. The beam is then charge-state analyzed by 80-cm long electrostatic deflection plates. After being separated horizontally by 1–2 cm, the different charge states are detected in two scintillator-photomultiplier counters. The two detectors each have a sensitive area of 2.4 by 4.8 cm and are separated by a 3-mm-wide gap. The ionized charge state (e.g., C^{6+}) is detected in one of the counters (detector 1), while the other one detects the incident charge state as well as the very weak capture charge state (e.g., C^{4+}). The beam is focused so that it is approximately 5 mm high and 1 mm wide. Thereby a 10:1 ratio between charge-state separation and individual charge-state width can be obtained. The ratio of the number of counts in the background between the two charge-state peaks to the number of counts in the incident charge state is less than 0.03%. The two scintillator-photomultiplier detectors each consist of a rectangular piece of scintillator material [27] which is glued to a wedge-shaped piece of lucite. For better light collection, a thin film of aluminum, approximately 1.4–mg/cm^2 thick, is evaporated onto the scintillator. Since we are interested in the ratio of the number of counts in detector 1 to the number of counts in both detectors, we do not have to know the absolute collection efficiencies of these detectors. However, their relative efficiency was tested for each incoming ion beam and energy and was found to be equal to unity to better than ±3%.

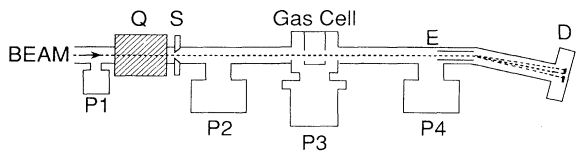

FIG. 2. Sketch of the Stanford Van de Graaff beam line used. The symbols have the following meaning: *P*1–*P*4, pumps; *Q*, quadrupole magnet; *S*, four-jaw slits; *E*, electrostatic deflection plates; *D*, detector chamber.

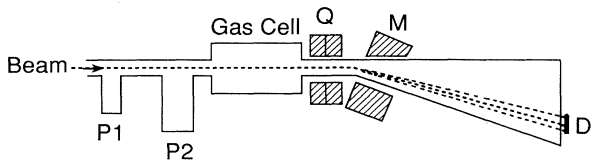

FIG. 3. Sketch of the LBL Bevatron beam line used. The symbols have the same meaning as in Fig. 2; *M* is a dipole magnet.

At the Lawrence Berkeley Labortory's Bevatron accelerator we have measured one-electron-loss cross sections for 100- and 380-MeV/nucleon Au^{52+} projectiles in collisions with H_2, He, C, and N_2 targets, 380-MeV/nucleon Au^{75+} and U^{86+} projectiles in collisions with H_2 and N_2 targets, and 405-MeV/nucleon U^{90+} projectiles on a H_2 target. Figure 3 shows a schematic of the beam line used. The ion beam provided by the Bevatron accelerator is pulsed with a repetition rate of 10 to 15 pulses per minute. The length of the individual pulses can be varied within small limits; for our experiments the pulse length was 100 msec. The focusing of the beam is accomplished by a series of magnets upstream from the target-gas cell. However, because of the divergence of the beam, as well as its width, only about 1% of the beam is transmitted through the gas cell. This fraction is analyzed by a pair of dipole magnets. Between the gas cell and the dipole magnets, the beam passes through a pair of focusing quadrupole magnets. The charge-state beams, separated by about 4.5 cm near charge state 52+

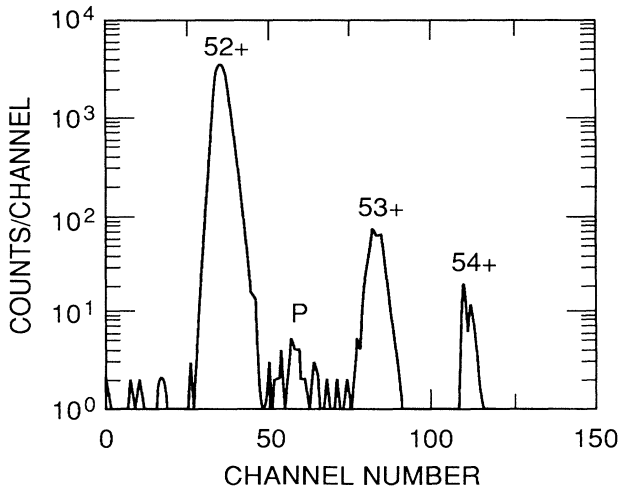

FIG. 4. *X*-position spectrum for 380-MeV/nucleon Au^{52+} incident on H_2 at 149-mTorr pressure. The emerging Au charge-state peaks are shown, as well as a pile-up peak *P*.

and less for higher charge states, pass through a thin Mylar window at the end of the beam line and enter a 25-cm-wide and 10-cm-high position-sensitive multiwire proportional counter, which sits in air. The beam was usually focused so that the charge states were 15 to 20 mm high and 3 to 7 mm wide, resulting at best in an approximately 7:1 ratio of charge-state separation to individual charge-state width. The multiwire proportional counter we used is a modified version of a detector used by Schweppe [28]. It consists of three flat, parallel electrodes, an anode, and two cathodes for the x- and y-position readout. The cathodes are of the so-called "graded-density" type, where the cathode wires are electrically connected into two groups such that the density of each group changes in an approximately linear manner across the entire cathode width [29]. The position resolution is 1 mm for the x cathode, and 4 mm for the y cathode.

Figure 4 shows an x-position spectrum for 380-MeV/nucleon Au^{52+} incident on H_2 at 149-mTorr pressure. The three detected charge states are Au^{52+}, Au^{53+}, and Au^{54+}. The small peak in between the incident and the first ionized charge state of the x spectrum is a result of pile-up. By reducing the number of particles per pulse from 100 to 20, we observed that the pile-up peak disappears. Since a reduction of the beam intensity by a factor of 5 was impractical, we devised a method of including the pile-up peaks in our data analysis [30]. As was the case in the Van de Graaff experiment, we do not need to know the absolute counting efficiency of the detector. The relative efficiency was determined by moving two charge states across the width of the detector and measuring their relative ratios. We found the relative efficiency to be constant within $\pm 8\%$.

The quality of the cross-section measurements for both the Van de Graaff and the Bevatron accelerator experiments relies heavily on the purity of the target gases and the knowledge of the physical properties of the gas cells. The gas purity is important because the cross section for projectile electron loss is roughly proportional to $Z_t^2+Z_t$, where Z_t^2 stems from the target nucleus and Z_t from the target electrons. This implies, that for gases like hydrogen or helium, where the electronic contribution to the electron-loss cross section might be detectable, high-Z_t impurities like water or nitrogen molecules can falsify the measured cross section if their concentration becomes too high. Therefore, we decided to use high-purity target gases [31]. Using the simple $Z_t^2+Z_t$ scaling, we calculate that the total effect of these impurities results in a less than 3% increase for the high-purity H_2 and He used, compared to a 15% increase for commercial hydrogen. During the Van de Graaff accelerator experiment, we compared the two hydrogen targets and found an increase in the cross section of approximately 10%, which is consistent with our theoretical estimate.

The purity of the target gases is determined not only by their "intrinsic" contamination, but also by the outgassing of high-Z_t molecules from the inner walls of the gas cell. Most of this contamination is water and nitrogen, and the amount of contamination is proportional to the surface area of the gas cell. With the Van de Graaff experiment, the setup did not allow for baking, so the gas cell was kept under vacuum for weeks before the actual experiments started. Under these conditions, the flow rate due to outgassing is 10^{-4} Torr liter/sec [32], whereas the calculated target-gas flow rate is six to seven orders of magnitude larger and, therefore, the contamination due to outgassing can be neglected. While the Van de Graaff experiment gas cell has a surface area of approximately 200 cm^2, the surface area of the Bevatron experiment gas cell amounts to about 26 000 cm^2. Here, the outgassing presents a much bigger problem and the gas cell has to be baked to reduce the effect of contaminations. By using a mass spectrometer, we determined the outgassing rates and the partial pressures for various background gases before and after baking the gas cell for about 24 h at approximately 160 °C. We measured a reduction of the rate from approximately 10^{-5} to 10^{-7} Torr liter/sec. Comparing the latter value with the measured target-gas flow rates of 0.1 to 1 Torr liter/sec during the experiment leads us to the conclusion that the contamination due to outgassing has been reduced to negligible proportions.

In the case of the Van de Graaff experiment gas cell, the biggest systematic error, between 5% and 10%, in the final determination of the electron-loss cross section arises from the uncertain effective length of the target-gas cell. Details of the effective-length determination are given in Appendix A. Since in the Bevatron experiment the expected electron-loss cross sections are more than an order of magnitude smaller than the cross sections measured in the Van de Graaff experiments, the number density of the target atoms had to be increased accordingly. To achieve this, we designed a gas cell, 241 cm long and 40 cm in diameter. Details about this target-gas cell are given in Appendix B. In both the Van de Graaff and the Bevatron experiments the effect of temperature variations introduces an uncertainty of less than 1%. The total experimental uncertainties in the two experiments are less than $\pm 11\%$ [30], caused mainly by target length uncertainties in the Van de Graaff experiment and by relative detector efficiency uncertainties in the Bevatron experiment.

IV. DATA ANALYSIS

In our experiments we measure for a given projectile and energy the number of particles n_i in a given charge state as a function of the target-gas pressure. From these numbers, the charge-state fractions f_i can be computed in a straightforward way by taking the ratio

$$f_i = n_i \Big/ \sum_j n_j \ . \tag{13}$$

In the Van de Graaff experiment, these fractions are measured for six to eight different target-gas pressures for which they generally remain below 5% of the initial charge state. In the Bevatron experiment, they are measured at two to eight pressures. The charge-state fractions depend on the target thickness x and on the charge exchange cross sections σ_{ji} from charge state j to charge state i. The individual fractions are connected through a system of coupled differential equations

$$\frac{df_i}{dx} = \sum_{j\,(\neq i)} (\sigma_{ji} f_j - \sigma_{ij} f_i) \ . \tag{14}$$

An exact solution of this system of coupled differential equations can be obtained only numerically. However, for small target thicknesses an approximate solution to these equations is given by [33]

$$f_i = f_i(0) + \sigma_{i-1,i} x - (\sigma_{i-1,i}\sigma_{i,i+1} + \sigma_{i-1,i}\sigma_{i,i-1}) x^2 \ . \tag{15}$$

The first term $f_i(0)$ is the background yield due to electron loss in the residual beam line vacuum, incomplete charge-state selection by the magnets, or slit-edge scattering at the collimators. In most cases, the background yield was much less than 0.5%. The next term is linear in the target thickness and it is this term we use to determine the electron-loss cross section. For the Van de Graaff data, a linear least-square fit suffices to obtain the cross section. For the highest gas pressures, the Bevatron data exhibit the presence of the quadratic term in Eq. (15) which is due to two-step charge-transfer processes. We analyzed this data with a quadratic fit for the whole set and a linear fit at the lowest pressures, where the charge-state fraction is still a linear function of the pressure. Both fits agreed within 3%.

The target thickness x which we use to calculate the cross section is measured in number of molecules per cm^2 and derived from the ideal-gas law

$$x = N_A P l / RT = 9.65 \times 10^{15} P l / T \ , \tag{16}$$

where N_A is Avogadro's number, P is the pressure in mTorr, l is the target length in cm, T is the temperature in K, and R is the universal gas constant.

The total uncertainty involved in the data analysis alone, including statistical and systematic errors, is less than ±4% for the Li^{2+}, C^{5+}, and O^{7+} projectiles, less than ±7% for the Au^{52+} and U^{86+} projectiles, and less than ±41% for the Au^{75+} projectile [30]. The reason for the large error in the latter case is discussed below.

V. RESULTS

In the Introduction, we mentioned experiments other than projectile or target ionization which investigate the electron-electron interaction in ion-atom collisions. Several different experiments display the presence of this interaction [10–16]. While most require rather elaborate experimental techniques, few attempts have been made to investigate the effect with comparatively simple projectile [34–37] or target [38] ionization measurements. Some of these experiments [36, 38] exhibit a qualitative agreement with the theoretical predictions [4]. We did not study target ionization because here the analysis of the experiments is complicated by two competing processes, the direct ionization of the target and the capture of a target electron by the projectile. The advantage of studying projectile ionization is that capture of a projectile electron by the target is absent due to the lack of vacancies in the target atom [33].

Starting with the lowest-Z_p projectiles we used, Fig. 5 compares our experimental results for Li^{2+} on H_2 and He with our theoretical calculations. The error bars include the experimental and data analysis uncertainties. The arrow on the abscissa of Fig. 5 and the subsequent figures indicates the projectile energy corresponding to the threshold given by Eq. (11). For the Li^{2+} on H_2 collision system we also show low-energy data by Shah, Goffe, and Gilbody [39] and Shah and Gilbody [40]. The solid line in Fig. 5(a), and for all other H_2 target systems, is based on the calculation of Ref. [25] for a molecular hydrogen target. The solid line in Fig. 5(b) is the screening-antiscreening calculation, based on Eq. (12) for helium, where the target form factor is given by the analytic expression in Eq. (10) with an effective charge of $\alpha = 1.69$.

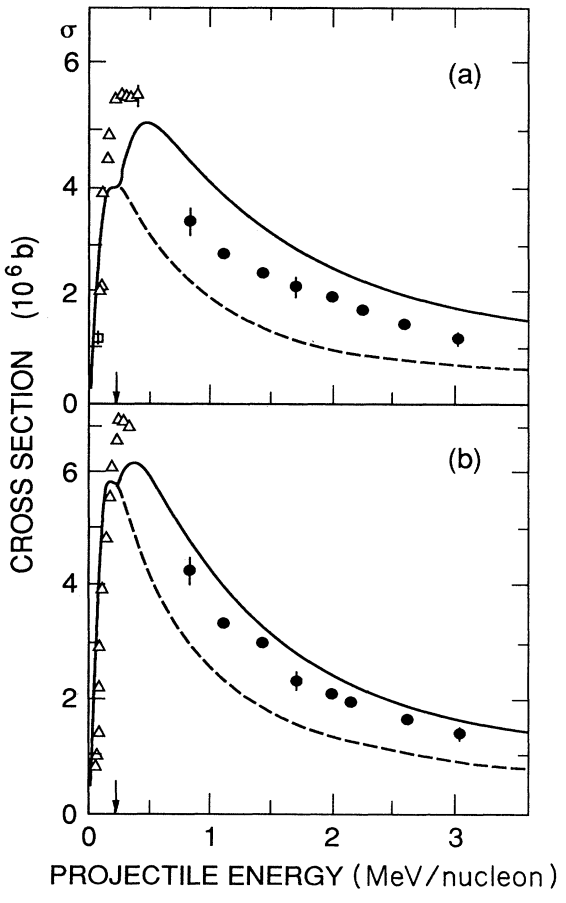

FIG. 5. Projectile electron-loss cross sections for Li^{2+} incident (a) on H_2 and (b) on He. □, Δ, data from Refs. [39] and [40]; ●, our results. The arrow on the abscissa indicates the projectile energy corresponding to the threshold given by Eq. (11). In (a) the solid curve is the screening-antiscreening calculation for H_2 and the dashed curve is the screening part. In (b) the solid curve is the screening-antiscreening calculation for He and the dashed curve is the screening part.

The dashed curves are the screening parts of the cross sections. A discussion of the limit of validity of the PWBA is also given in Ref. [25]. In the case of $Li^{2+}+H_2$, the PWBA is not valid below 0.2 MeV/nucleon, but above this energy the screening-antiscreening calculations agree reasonably well with the experimental results.

For heavier projectiles like C^{5+} and O^{7+}, the energies available at the Stanford Van de Graaff accelerator (0.75 to 3.5 MeV/nucleon) span the range below and above the threshold. These projectiles also carry a higher nuclear charge which should make the comparison with the theory more favorable since the PWBA assumes $Z_t \ll Z_p$, and molecular effects are very small [25]. Figures 6 and 7 compare our experimental results with the theoretical calculations. Also shown are experimental data from Ref. [34] for C^{5+} on H_2 and Ref. [35] for C^{5+} on He and for O^{7+} on H_2 and He. Our results for both C^{5+} and O^{7+} are in excellent agreement with the screening-antiscreening theory.

As mentioned in Sec. III, the biggest source of error in the Van de Graaff experiments is the systematic uncertainty in the effective gas-cell length. Therefore, by taking the ratios of H_2 to He cross sections, one can significantly reduce the size of the error bars. Figure 8 shows the experimental and theoretical cross-section ratios for Li^{2+}, C^{5+}, and O^{7+}. The solid line gives the ratio of the screening-antiscreening calculations and the dashed line the ratio of the nuclear PWBA calculations. Our experimental values follow closely the screening-antiscreening curves.

At the Lawrence Berkeley Laboratory's Bevatron accelerator we were able to study one-electron loss of many-electron projectiles by using Au and U ion beams. Figures 9 and 10 show one-electron-loss cross sections for Au^{52+} in collisions with H_2, He, C, and N_2 targets at 100 and 380 MeV/nucleon. Both energies lie above the electron-electron threshold. In Fig. 9 and all subsequent

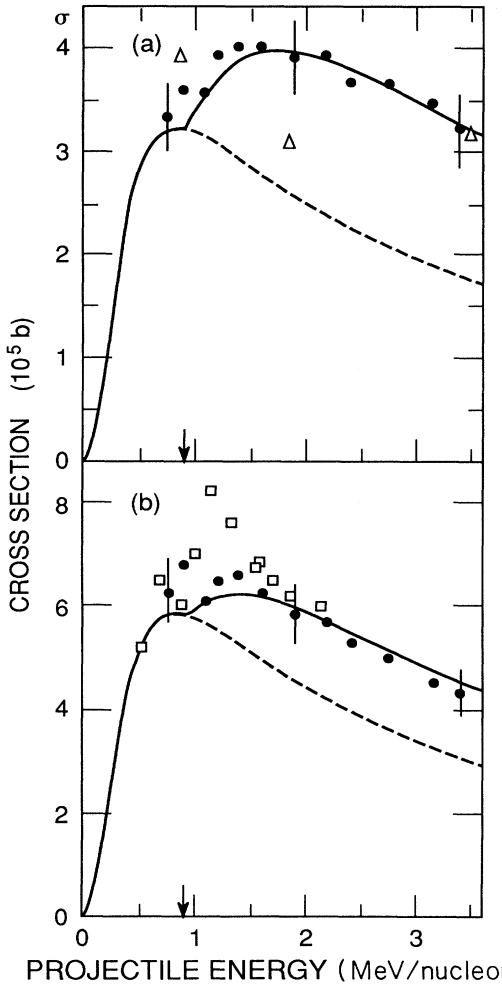

FIG. 6. Projectile electron-loss cross sections for C^{5+} incident (a) on H_2 and (b) on He. Δ, data from Ref. [34]; □, data from Ref. [35]; ●, our results. The curves are calculated as for Fig. 5.

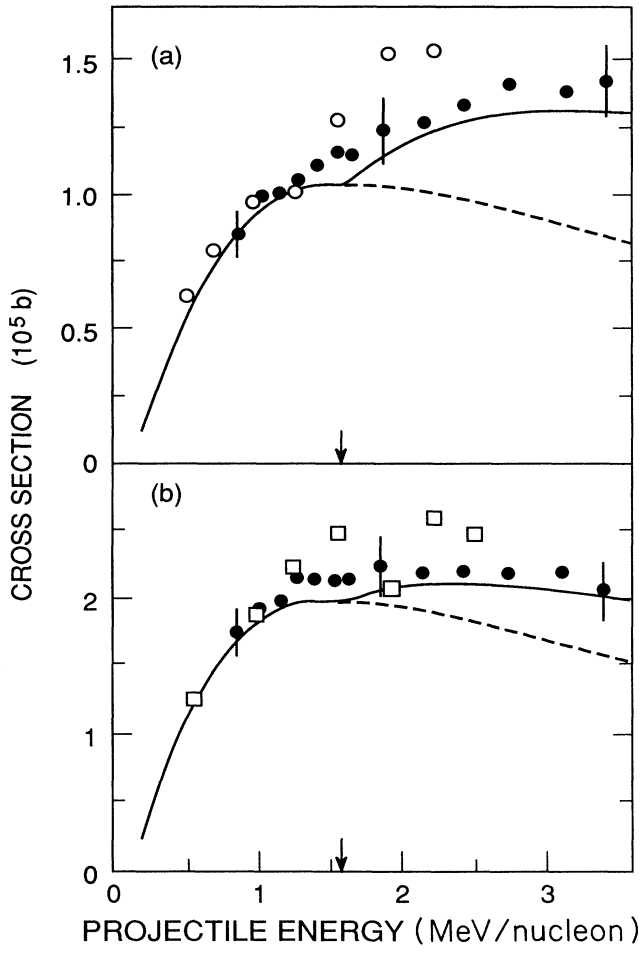

FIG. 7. Projectile electron-loss cross sections for O^{7+} incident (a) on H_2 and (b) on He. ○, □, data from Ref. [35]; ●, our results. For clarity, data points from Refs. [36] and [37] have been omitted. The curves are calculated as for Fig. 5.

figures, the solid curves are the screening-antiscreening calculations summed over the relevant projectile subshells, using Slater screening constants for the effective nuclear charges and the subshell binding energies of Carlson *et al.* [41] for partially stripped ions. The solid curve in Fig. 10(a) is the screening-antiscreening calculation for the nitrogen atom times two. The dashed curves represent the screening parts of the cross sections, which for these high-Z ions are essentially identical with the nuclear cross sections. The experimental data points agree well with the theory for Au^{52+} on H_2 and also for Au^{52+} on He. For Au^{52+} on C and N_2, antiscreening produces a relatively small change in the cross section, which cannot be ascertained experimentally. A comparison with the $Au^{52+}+C$ results shows that solid-state effects are absent for these light targets, as already noted by Anholt and Meyerhof [42].

We also attempted to measure the cross section for Au^{75+} on H_2 and N_2 at 380 MeV/nucleon. This measurement is more difficult than the previous one. The main reason is the high background contribution due to slit-edge scattering. As mentioned previously, it is not possible to focus the Bevatron ion beam sufficiently so that it will not hit the stainless-steel entrance or exit colli-

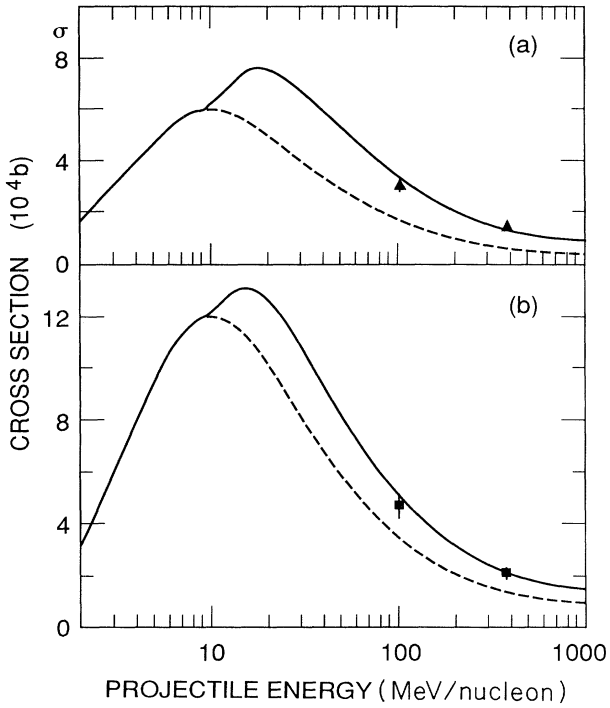

FIG. 9. Projectile one-electron-loss cross sections for Au^{52+} (a) on H_2 and (b) on He. The solid curves are calculated, as described in the text. The dashed curves are the screening parts.

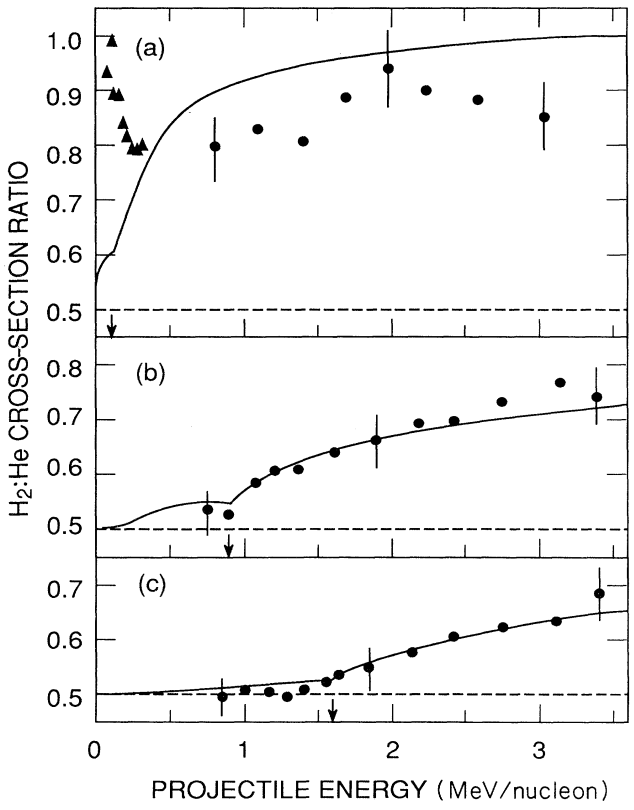

FIG. 8. Ratio of H_2 to He cross sections (a) for Li^{2+}, (b) for C^{5+}, and (c) for O^{7+}. ▲ , data from Ref. [40]; ●, our results. The solid curves are the ratios of the molecular H_2 to the He calculations and the dashed curves are the ratios of the nuclear PWBA calculations.

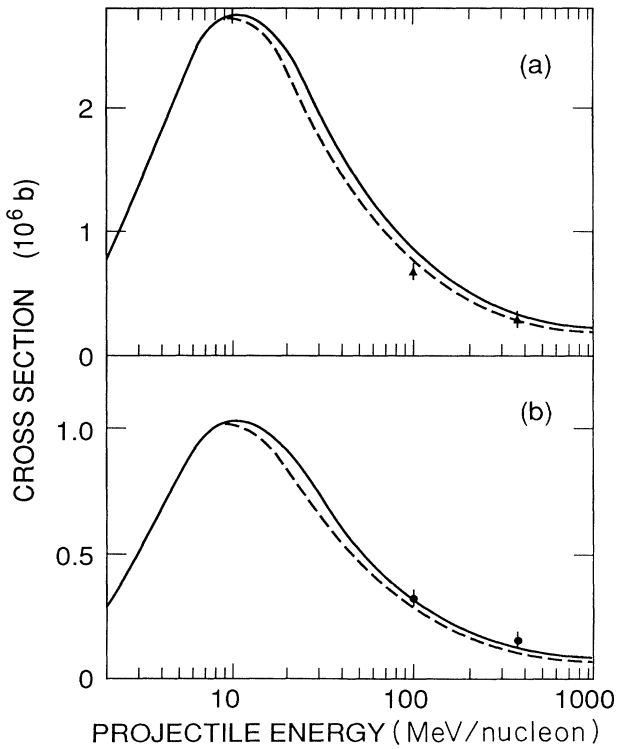

FIG. 10. Projectile one-electron-loss cross sections for Au^{52+} incident (a) on N_2 and (b) on C. The solid curves are the atomic screening-antiscreening calculations, as described in the text, multiplied by two for N_2, and the dashed curves are the screening parts.

mators of the gas cell. As part of the beam collides with these apertures, it changes its charge state. The most likely charge-state distribution produced in Au^{75+} + Fe collisions at this energy unfortunately centers around charge states 75+ and 76+. The same is true for the Au^{52+} experiment, but there worked in our favor because this charge-state region is far removed from the slit-scattered charge states. Figure 11 shows the measured and calculated cross sections for Au^{75+} on H_2 and N_2. Unfortunately, the statistical uncertainties of the measured cross sections are too large to allow a meaningful comparison with theory.

Figure 12 gives the results for U^{86+} on H_2 and He. Here again, we find good agreement between the measured cross sections and the screening-antiscreening theory for both H_2 and He targets.

We tried to measure the one-electron cross section for U^{90+} on H_2 at 405 MeV/nucleon, because at this energy Claytor *et al.* [10] had determined the electron-loss cross section of few-electron U ions, including U^{90+}, channeled in a Si crystal. In principle, the channeling experiment should provide an electron-impact ionization cross section for U^{90+}, which should be related to the antiscreening cross section in $U^{90+}+H_2$ collisions, although not close to the electron-electron threshold. We discuss this point in a forthcoming paper [43]. But, as Fig. 13 shows, our present measurement was much too imprecise to extract an antiscreening cross section, because the cross

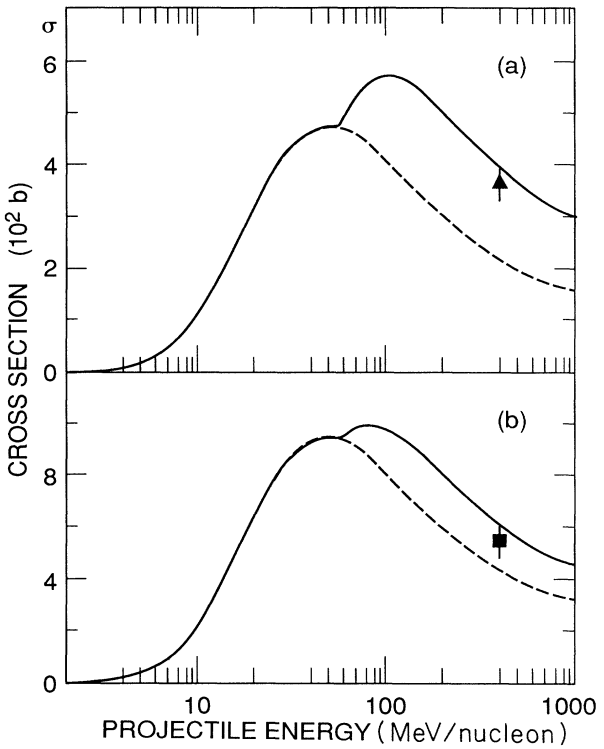

FIG. 12. Projectile one-electron-loss cross sections for U^{86+} incident (a) on H_2 and (b) on He. The curves are calculated as for Fig. 9.

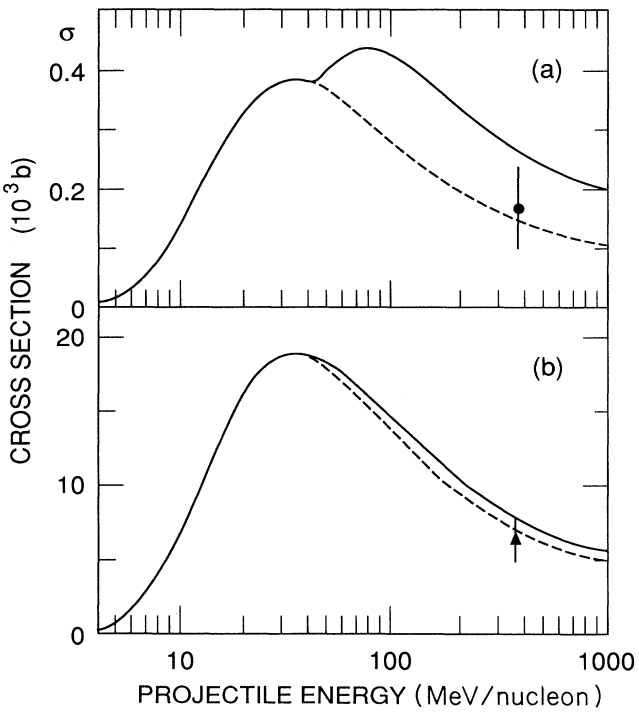

FIG. 11. Projectile one-electron-loss cross sections for Au^{75+} incident (a) on H_2 and (b) on N_2. The curves are calculated as for Fig. 9, except that the curves for N_2 are the atomic calculations multiplied by two.

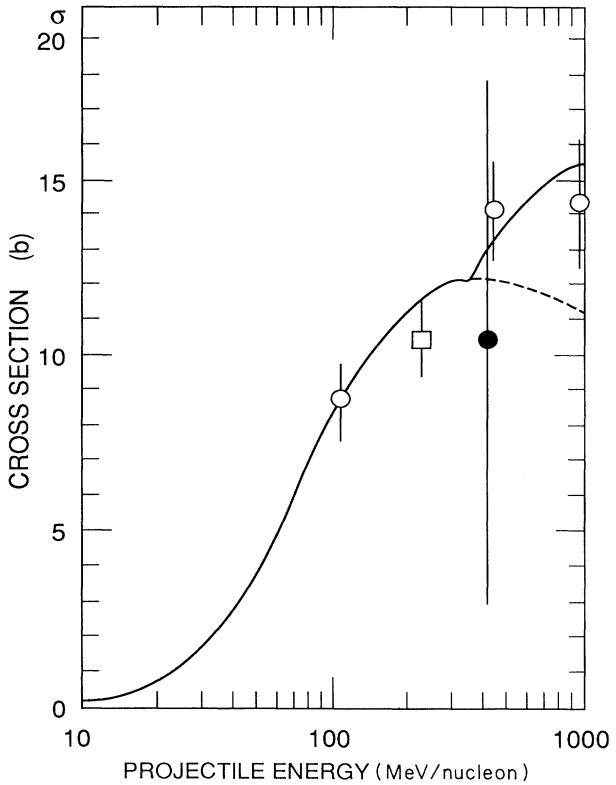

FIG. 13. Projectile one-electron-loss cross sections for U^{90+} incident on H_2 (●). The open symbols are cross sections scaled from U^{90+} (○) and U^{91+} (□) incident on Be (Ref. [43]).

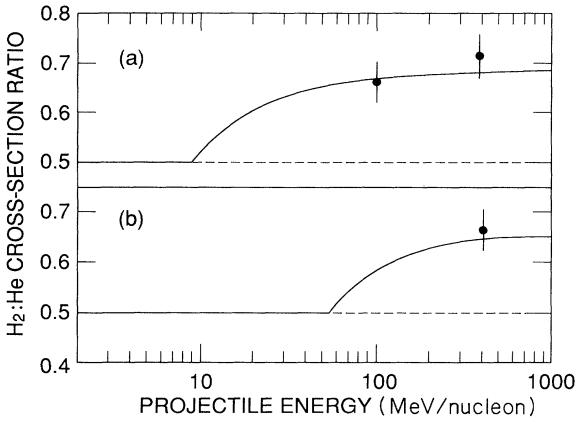

FIG. 14. Ratio of H_2 to He cross sections (a) for Au^{52+} and (b) for U^{86+}. The solid curves are the ratios of the "Stewart" molecular model for H_2 to the He screening-antiscreening calculations and the dashed curves are the ratios of the nuclear PWBA calculations.

section is so small and the corresponding background under the charge fraction peak is large. Nevertheless, to check the accuracy of the theory, we scaled one-electron-loss cross sections for U^{90+} and U^{91+} on Be from Ref. 44 to a H_2 target by applying a factor $\frac{2}{16}$ to the $U^{90+}+Be$ cross section and twice that for U^{91+}. This procedure should be valid below the electron-electron threshold where the cross section is essentially nuclear, i.e., proportional to Z_t^2. Above the threshold, this scaling is not valid because the antiscreening cross section is proportional to the number of target electrons. Agreement between theory and experiment is satisfactory over the energy range shown in Fig. 13.

In Fig. 14 we show the ratio of the H_2 and He cross sections for Au^{52+} and U^{86+}. The solid lines are the screening-antiscreening ratios and the dashed line the nuclear PWBA ratios. The agreement between the screening-antiscreening calculations and the experimental ratios is very good.

VI. CONCLUSIONS

The goal of this work has been to investigate the effect of target electrons on the projectile electron-loss cross section. The target electrons can act not only coherently by screening the target nucleus but they may also act incoherently by directly ionizing a projectile. We showed that this screening-antiscreening effect is important for targets with a low nuclear charge, since the cross section for a neutral target is roughly proportional to $Z_t^2+Z_t$, where Z_t^2 is the contribution due to the target nucleus and Z_t comes from the target electrons. In order to investigate the screening-antiscreening effect, we have measured and calculated cross sections for Li^{2+}, C^{5+}, and O^{7+} on H_2 and He, Au^{52+} on H_2, He, C, and N_2, Au^{75+} on H_2 and N_2, U^{86+} on H_2 and He, and U^{90+} on H_2. The corresponding calculations have been performed in the plane-wave Born approximation.

We have not only been able to demonstrate unambiguously the effect of the interaction between target and projectile electrons over a wide range of projectiles and collision energies, but we have also shown that this interaction can lead to a significant increase in the projectile electron-loss cross section. The largest increases relative to the nuclear PWBA cross section which we have been able to observe are 80–90 % for 1–3-MeV/nucleon Li^{2+} and 70–80 % for 380-MeV/nucleon Au^{52+} on H_2.

ACKNOWLEDGMENTS

We are grateful to Dr. M. B. Shah for providing new data on $Li^{2+}+H_2$ electron loss prior to publication and to Dr. A. S. Schlachter for assistance during the data acquisition (LBL). This work was supported in part by the National Science Foundation Grant No. PHY-8614650 (Stanford University); by the Director, Office of Energy Research, Office of Basic Energy Sciences, Chemical Sciences Division; and Office of High Energy and Nuclear Physics, Nuclear Physics Division, U.S. Department of Energy under Contract No. DE-AC-76SF00098 (LBL); and by the U.S. Department of Energy under Contract No. DE-AC02-76CH00016 (BNL). One of us (K.S.) was supported by a grant from the Research Corporation. Another one of us (L.B.) was supported by the Bourse Lavoisier from the Ministère des Affaires Étrangers (France) and by the International Federation of University Women.

APPENDIX A

In the following, we present details of the effective-length determination for the Van de Graaff experiment target-gas cell. The base pressure in the beam-line sections upstream and downstream of the gas cell is in the lower 10^{-6}-Torr range. Due to the finite pumping speed of the diffusion pump (*P*3 in Fig. 2), the pressure in the differentially pumped area depends on the target-gas pressure. At the maximum gas-cell pressure used (450 mTorr of H_2), the pressure in the differentially pumped area is in the lower 10^{-3}-Torr range. The entrance and exit apertures to the 6-cm-long gas cell have an area of 2 and 12 mm^2, respectively. The apertures are contained in tubes, 18 mm long with an inner diameter of 7 mm. Since the target gas streams out through these apertures and tubes, the net result of this gas flow will be an increased effective length of the gas cell. For the gas pressures used in the Van de Graaff experiments (5–450 mTorr), the gas flow is in the transitional flow regime [45], i.e., between viscous and molecular flow. Following the discussion of this flow regime in Ref. [45], the conductance of a system measured in liters per second can be approximated by the sum of viscous and molecular conductances

$$C=C_{\text{viscous}}+C_{\text{molecular}}$$
$$=3.27\times10^{-2}\frac{P_{\text{av}}}{\eta}\frac{d^4}{l}+\frac{65.8}{\sqrt{M}}\frac{d^3}{d+\frac{3}{4}l}\ , \qquad \text{(A1)}$$

where P_{av} (Torr) is the average pressure in the system, η

(poise) is the viscosity of the gas and M (amu) the mass of a gas molecule, l (cm) is the length of the system and d (cm) its typical diameter. Using Eq. (A1) we can calculate the conductances of apertures and tubes and add them according to

$$C_{\text{total}}=\frac{C_{\text{aperture}}C_{\text{tube}}}{C_{\text{aperture}}+C_{\text{tube}}} . \tag{A2}$$

Knowing the gas-cell pressure P_0 as well as the pressure in the differentially pumped area P_d, we can estimate how the pressure drops from P_0 to P_d over the distance $l_{\text{aperture}}+l_{\text{tube}}$. Segmenting this distance into finite intervals δl_i we can then calculate the effective length of the gas cell

$$l_{\text{eff}}=l_0\left[\frac{\sum_i P_i\delta l_i}{P_0}\right]_{\text{entrance}}+\left[\frac{\sum_i P_i\delta l_i}{P_0}\right]_{\text{exit}} . \tag{A3}$$

For H_2 and He, the result of this estimate is an effective length of 7.3 and 7.1 cm, respectively, for the range of pressures used in this experiment. The difference between the two results is due to the difference in mass and viscosity. Equation (A1) is only an approximation of the true conductance. By making different assumptions about the gas flow, which are based on a discussion in Ref. [45], we estimate that the uncertainty in the effective gas-cell length is between 5% and 10%.

APPENDIX B

Here we present a brief overview of the Bevatron experiment target-gas cell and its operation. The cell is 241 cm long and has a diamenter of 40 cm. The entrance and exit apertures to the gas cell are 5-cm-long tubes, 6 mm in diameter. The tubes can be sealed with flappers as depicted in Fig. 15. These flapper valves are opened with a solenoid and closed by a spring. The whole arrangement sits in vacuum and the solenoids can be controlled from the outside. The flapper valves are ideal for the Bevatron since a beam pulse comes only every 4 sec. Therefore, the valves can be opened for about twice the duration of the beam pulse, i.e., about 200 msec, and they can remain closed for the rest of the time. This arrangement allows for very high target-gas pressures to be used (up to 5 Torr of H_2 and 6 Torr of N_2), while the rest of the beam line remains under high vacuum. The flapper valves are controlled by an electronic circuit which is triggered by a signal from the Bevatron whenever the beam is directed into the beam line. Figure 15 also shows the timing sequence of the flapper valves. The timing circuit enables us to continuously vary the duration of time for which the flapper valves are open. The actual times for opening (2 msec) and closing (15 msec) have been measured with a photodiode and a photomultiplier on either side of the valve. The overall timing has been adjusted to assure

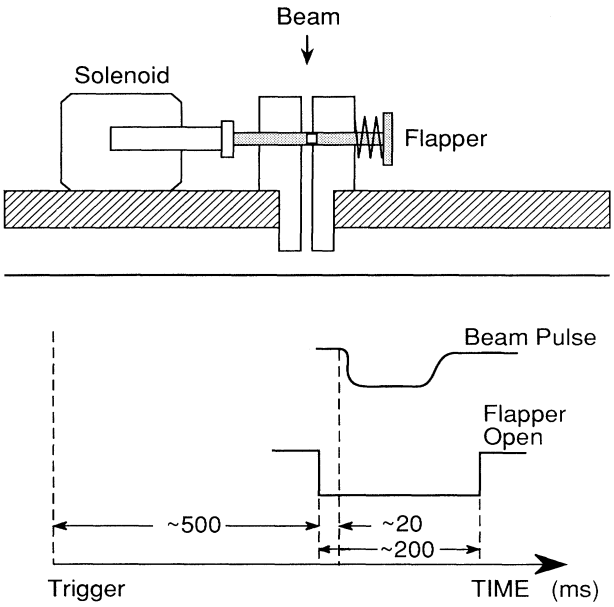

FIG. 15. Sketch of the flapper valve and a schematic diagram of the flapper-valve timing sequence.

that the beam will not hit the flapper.

The target gas enters the gas cell through a flow control valve and is evacuated from the gas cell on the opposite side by a turbo-molecular-pump, not shown in Fig. 3, whose effective pumping speed can be varied by a coarse needle valve located between the pump and the cell. A Baratron readout serves as an input to the flow controller, where it is continuously compared with a reference voltage which can be set by the experimenter. The resulting error signal either opens or closes the flow control valve. After some adjustment to the internal timing constants of the control unit, we have been able to stabilize the pressure to better than 2% for values between 20 and 100 mTorr and to better than 1% for values above 100 mTorr. It takes this system approximately 5 min to reach a stable pressure. The equilibrium pressure distribution inside the gas cell has been determined experimentally and was found to be uniform to better than 1%. During the time when the flapper valves are open, gas streams out of the entrance and exit tubes which will result in a pressure drop inside the gas cell. To minimize this effect, we decided to give the cell a large volume. To a first approximation the pressure inside the cell will fall off exponentially with a time constant which is given by the ratio of the cell volume V to the duty-cycle ($\mathcal{C}_{\text{duty}}$) averaged conductance of the two flapper valves C_{fv},

$$P(t)=P_0\exp(-2C_{fv}t\mathcal{C}_{\text{duty}}/V) . \tag{B1}$$

For a pressure of 5 Torr of H_2 gas, Eq. (B1) predicts a drop in gas-cell pressure after 200 msec of less than 3%.

*Present address: Leybold Aktien Gesellschaft, Wilhelm Rohn Strasse 25, 6450 Hanau 1, Germany.
†Present address: Institut Curie, Section Physique et Chimie, 11 rue Pierre et Marie Curie, 75005 Paris, France.
‡Present address: Naval Surface Warfare Center, R-41 White Oak Laboratory, Silver Spring, MD 20903-5000.
§Present address: National Institute of Standards and Technology, Quantum Meterology Divison, Gaithersburgh, MD 20899.

[1] D. R. Bates and G. Griffing, Proc. Phys. Soc. London Ser. A **66**, 961 (1953).
[2] D. R. Bates and G. Griffing, Proc. Phys. Soc. London Ser. A **67**, 663 (1954).
[3] D. R. Bates and G. Griffing, Proc. Phys. Soc. London Ser. A **68**, 90 (1955).
[4] J. H. McGuire, N. Stolterfoht, and P. R. Simony, Phys. Rev. A **24**, 97 (1981).
[5] T. Shirai, K. Iguche, and T. Watanabe, J. Phys Soc. Jpn. **42**, 238 (1977).
[6] M. Inokuti, Rev. Mod. Phys. **43**, 297 (1971).
[7] N. Stolterfoht, in *Spectroscopy of Few-Electron Ions,* edited by V. Florescu and V. Zoran (World Scientific, Singapore, 1989), p. 324; Phys. Scr. **42**, 192 (1990); in U.S.–Japan Seminar on Dynamic Excitation by Exotic and Highly Charged Ions, Anchorage, 1990 [Nucl. Instrum. Methods (to be published)].
[8] H.-P. Hülskötter, W. E. Meyerhof, E. Dillard, and N. Guardala, Phys. Rev. Lett. **63**, 1938 (1989).
[9] J. H. McGuire, in *Advances in Atomic, Molecular, and Optical Physics,* edited by D. R. Bates and B. Bederson (Academic, Orlando, 1991), Vol. 29, p. 217.
[10] N. Claytor, B. Feinberg, H. Gould, C. E. Bemis, J. G. del Campo, C. A. Ludemann, and C. R. Vane, Phys. Rev. Lett. **61**, 2081 (1988).
[11] S. Andriamonje, R. Anne, N. V. de Castro Faria, M. Chevallier, C. Cohen, J. Dural, M. J. Gaillard, R. Genre, M. Hage-Ali, R. Kirsch, A. L'Hoir, B. Farizon-Mazuy, J. Mory, J. Moulin, J. C. Poizat, Y. Quéré, J. Remillieux, D. Schmaus, and M. Toulemonde, Phys. Rev. Lett. **63**, 1930 (1989).
[12] A. L' Hoir, S. Andriamonje, R. Anne, N. V. de Castro Faria, M. Chevallier, C. Cohen, J. Dural, M. J. Gaillard, R. Genre, M. Hage-Ali, R. Kirsch, B. Farizon-Mazuy, J. Mory, J. Moulin, J. C. Poizat, Y. Quéré, J. Remilleux, D. Schmaus, and M. Toulemonde, Nucl. Instrum. Methods Phys. Res. B **48**, 145 (1990).
[13] T. J. M. Zouros, D. H. Lee, and P. Richard, Phys. Rev. Lett. **62**, 2261 (1989).
[14] P. Richard, in *X-Ray and Inner-Shell Processes, Knoxville, 1990,* Proceedings of the Conference on X-Ray and Inner-Shell Processes, AIP Conf. Proc. No. 215, edited by T. A. Carlson, M. O. Krause, and S. T. Manson (AIP, New York, 1990), p. 315.
[15] J. A. Tanis, Phys. Rev. Lett. **53**, 2551 (1984).
[16] M. Schulz, J. P. Giese, J. K. Swenson, S. Datz, P. F. Dittner, H. F. Krause, H. Schöne, C. R. Vane, M. Benhenni, and S. M. Shafroth, Phys. Rev. Lett. **62**, 1738 (1989).
[17] E. Merzbacher and H. W. Lewis, in *Handbuch der Physik* (Springer, Heidelberg, 1958), Vol. 34, p. 166.
[18] R. Anholt, Phys. Lett. **114A**, 126 (1986).
[19] H. A. Bethe, Ann. Phys. (Leipzig) **5**, 325 (1930).
[20] Byung-Ho Choi, Phys. Rev. A **7**, 2056 (1973).
[21] D. H. Madison and E. Merzbacher, in *Atomic Inner Shell Processes* (Academic, New York, 1975), Vol. I, Chap. 1.
[22] I. M. Chesire and H. L. Kyle, Proc. Phys. Soc. (London) **88**, 785 (1966).
[23] J. H. Hubbell, W. J. Veigele, E. A. Briggs, R. T. Brown, D. T. Comer, and R. J. Howerton, J. Phys. Chem. Ref. Data **4**, 471 (1975).
[24] H. A. Bethe and R. Jackiw, *Intermediate Quantum Mechanics* (Benjamin-Cummings, Menlo Park, CA, 1968), p. 242.
[25] W. E. Meyerhof, H.-P. Hülskötter, Quing Dai, J. H. McGuire, and Y. D. Wang, Phys. Rev. A **43**, 5907 (1991).
[26] N. F. Mott and H. S. W. Massey, *The Theory of Atomic Collisions* (Oxford University Press, London, 1965), Sec. 3.1.
[27] The material was Bicron BC-404.
[28] J. Schweppe (private communication); J. Schweppe, A. Belkacem, L. Blumenfeld, N. Claytor, B. Feinberg, H. Gould, V. E.Kostroun, L. Levy, S. Misawa, J. R. Mowat, and M. H. Prior, Phys. Rev. Lett. **66**, 1434 (1991).
[29] E. Mathieson, G. C. Smith, and P. J. Gilvin, Nucl. Instrum. Methods **174**, 221 (1980).
[30] H.-P. Hülskötter, Ph.D. thesis, Stanford University, 1990 (unpublished).
[31] Gases supplied by Matheson Gas Products, Newark, CA.
[32] A. Roth, *Vacuum Technology,* 2nd ed. (North-Holland, Amsterdam, 1982), p. 144.
[33] R. Anholt, W. E. Meyerhof, H. Gould, C. Munger, J. Alonso, P. Thieberger, and H. E. Wegner, Phys. Rev. A **32**, 3302 (1985).
[34] R. Anholt, X.-Y. Xu, Ch. Stoller, J. D. Molitoris, B. S. Rude, and R. J. McDonald, Phys. Rev. A **37**, 1105 (1988).
[35] T. N. Tipping, J. M. Sanders, J. Hall, J. L. Shinpaugh, D. H. Lee, J. H. McGuire, and P. Richard, Phys. Rev. A **37**, 2906 (1988).
[36] R. Hippler, S. Datz, P. D. Miller, P. L. Pepmiller, and P. F. Dittner, Phys. Rev. A **35**, 585 (1987).
[37] S. A. Bowman, E. M. Bernstein, and J. A. Tanis, Phys. Rev. A **39**, 4423 (1989).
[38] R. D. Dubois and L. H. Toburen, Phys. Rev. A **38**, 3960 (1988).
[39] M. B. Shah, T. V. Goffe, and H. B. Gilbody, J. Phys. B **11**, L233 (1978).
[40] M. B. Shah and H. B. Gilbody, J. Phys. B **24**, 977 (1991).
[41] T. A. Carlson, C. W. Nestor, N. Wasserman, and J. D. McDowell, At. Data **2**, 63 (1970).
[42] R. Anholt and W. E. Meyerhof, Phys. Rev. A **33**, 1556 (1986).
[43] B. Feinberg, W. E. Meyerhof, H.-P. Hülskötter, A. Belkacem, D. W. Spooner, N. Guardala, E. Dillard, J. R. Alonso, G. F. Krebs, M. A. McMahan, B. S. Rude, L. Blumenfeld, H. Gould, J. Schweppe, K. Street, P. Thieberger, H. Wegner, and J. Rhoades-Brown (unpublished).
[44] R. Anholt, W. E. Meyerhof, X.-Y. Xu, H. Gould, B. Feinberg, R. J. McDonald, H. E. Wegner, and P. Thieberger, Phys. Rev. A **36**, 1568 (1987).
[45] S. Dushman, *Scientific Foundations of Vacuum Technique,* 2nd ed. (Wiley, New York, 1962), Chap. 2.